Chemical Shift Anisotropy and Offset Effects in Cross Polarization Solid-State NMR Spectroscopy

Srinivasan C. Shekar, Dong-Kuk Lee, and A. Ramamoorthy[1]

Department of Chemistry, Biophysics Research Division, and Macromolecular Science and Engineering, The University of Michigan,
930 N. University Avenue, Ann Arbor, Michigan 48109-1055

The effect of an offset term in the cross-polarization (CP) Hamiltonian of a heteronuclear spin-$\frac{1}{2}$ pair due to off-resonant radio frequency (rf) irradiation and/or chemical shift anisotropy on one of the rf channels is investigated. Analytical solutions, simulations, and experimental results are presented. Formulating the CP spin dynamics in terms of an explicit unitary evolution operator enables the CP period to be inserted as a module in a given pulse scheme regardless of the initial density matrix present. The outcome of post-CP manipulation via pulses can be calculated on the resulting density matrix as the phases and amplitudes of all coherence modes are available. Using these tools it is shown that the offset can be used to reduce the rf power on that channel and the performance is further improved by a post-CP pulse whose flip angle matches and compensates the tilt of the effective field on the offset channel. Experimental investigations on single crystalline and polycrystalline samples of peptides confirm the oscillatory nature of CP dynamics and prove the slowing down of the dynamics under offset and/or mismatch conditions.   © 2002 Elsevier Science (USA)

1. INTRODUCTION

During cross polarization (CP) (see the pulse sequence in Fig. 1), if the radio frequency (rf) irradiation field on a given channel is off-resonance, it results in an effective field tilted in the corresponding rotating frame (*1–9*). An obvious consequence is that the CP dynamics for the channel with the offset takes place about the tilted axis rather than in the x–y plane ($\mathbf{B}_0$ defining the z-axis) of the corresponding rotating frame. A closer look at the mathematical machinery of the evolution, driven by the CP Hamiltonian, reveals rich spin dynamics. This is brought about in the following fashion: the Hamiltonian for on-resonance CP in a doubly rotating, doubly tilted frame can be resolved into independent two-dimensional zero quantum (0Q) and double quantum (2Q) subspaces (*4, 5, 8–19*). Introduction of an offset term involving either spin introduces terms outside this block diagonal structure, fundamentally altering the course of evolution during CP. Study of the effects of rf offset(s) has an impressive history (*4, 6, 9, 16, 19–23*), addressing interesting

and important cases, although it has been relegated recently to the role of a minor detail (compared to the studies on the effects of "mismatch" of rf amplitudes and the rf phases, for example). More often than not, the offset terms are dropped in order to simplify the dynamical picture, which has its own merits and reflects many realistic situations. It should be noted that the offset can be introduced by the experimenter or it can naturally arise due to the chemical shift interaction; offset is inevitable for nonzero chemical shift anisotropy (CSA). If the magnitude of CSA is substantially larger than that of the heteronuclear dipolar coupling, which drives the coherence transfer in a CP experiment, the offset is impossible to ignore as it severely inhibits coherence transfer among the dipolar coupled heteronuclei.

On a practical note, CP is employed routinely in a wide variety of NMR experiments (*1–25*) spanning homonuclear and heteronuclear systems in solids and other anisotropic phases as well as in liquids. It is an indispensable unit in most solid-state NMR experiments in which the initial part invariably consists of coherence transfer from abundant nuclei to rare spins. A crucial step in CP is meeting the Hartman–Hahn (HH) match condition by rendering the nutation frequencies of both spin species equal in the doubly rotating frame upon adjusting the rf irradiation power levels. Conceptually simple and experimentally easy to implement, HH-match CP nevertheless places certain demands on rf power capabilities. When the HH-match condition is not fulfilled (that is the mismatch condition), the CP efficiency suffers, and for mismatches that are larger compared to the dipolar coupling the coherence transfer rapidly deteriorates. The mismatch is unavoidable in wet biological samples such as lipid bilayers as they are power lossy due to high water content. Furthermore, applying higher rf power ($\sim$1 kW) to such samples is technically demanding and, at the same time, the dissipated heat dehydrates the bilayer and can denature the sample. These shortcomings associated with the HH-mismatch problem can be offset to some extent by introducing offset rf irradiation in one or more channels such that the effective fields during the spin-lock period of the CP pulse sequence fulfill the HH-match condition.

Thus the twin motives for studying the effects of offset during CP are to uncover the rich dynamical details under these conditions and to continue in the previous vein to evaluate the unitary

[1] To whom correspondence should be addressed.
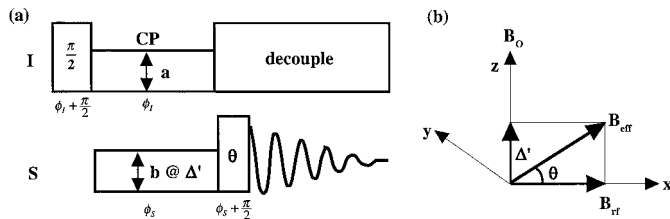
FIG. 1. (a) A cross polarization pulse sequence to obtain the S-spin chemical shift spectrum under the decoupling of I–S dipolar interaction. The transverse magnetization of I nuclei prepared by a $90°$ pulse with phase $\phi_I + \pi/2$ is locked using an rf pulse with phase ϕ_I and strength a on the I-spin channel, while a simultaneous rf pulse with phase ϕ_S and strength b at an offset Δ' is applied on the S-spin channel. At Hartmann–Hahn match, i.e., when $a = b$ and $\Delta' = 0$, the transverse magnetization of I nuclei is transferred to S nuclei via the I–S dipolar interaction. As shown in (b), an rf offset on the S-spin channel creates the effective field during CP along a tilted axis, $B_{\text{eff}} = \sqrt{(\Delta'^2 + B_{\text{rf}}^2)}$. Even in the presence of an rf offset, cross-polarization from I spins to S spins occurs when $B_{\text{eff}} = a$, while the transferred S magnetization is spin-locked along the B_{eff} direction. A post-CP pulse with a flip angle θ with a phase of $\phi_S + \pi/2$, when Δ' is nonzero, tilts the magnetization of S nuclei from the tilted axis, i.e., from the B_{eff} axis, to the transverse plane, where $\theta = \tan^{-1}(\Delta'/B_{\text{rf}})$. After the post-CP pulse, S-spin signal is acquired under the decoupling of I spins.

evolution operator for the CP period (to enable it to be inserted as a module in a given pulse sequence), and thus determine the resulting density matrix for an arbitrary initial condition (26), which in turn suggests procedures to overcome HH-mismatch problems. It turns out that in some respects the rf offset induces behavior similar to the HH-mismatch condition. Moreover, it is possible to use a corrective post-CP pulse along with the offset to enhance coherence transfer under HH-mismatch conditions. Further, an interesting feature pertaining to CP dynamics is uncovered in the course of these theoretical and experimental investigations: the rate of coherence transfer is slowed down due to the presence of offset and/or HH-mismatch conditions.

2. THEORY

We consider a pair of dipolar coupled heteronuclear spin-1/2 nuclei in the theoretical analysis of the paper. The CP Hamiltonian in a doubly rotating frame with an rf offset Δ' on the S-spin channel is (3, 4, 8, 10, 26) given by

$$H = R_Z(\phi_I, \phi_S)[aI_x + bS_x + \Delta(\Omega)S_z + d(\Omega)2I_zS_z]R_Z^\dagger(\phi_I, \phi_S), \quad [1]$$

where a and b are the rf irradiation strengths (in frequency units) with phases ϕ_I and ϕ_S on I- and S-spins respectively; $d(\Omega)$ is the heteronuclear dipolar coupling. The combination of all those interactions with S_z as the spin part of the Hamiltonian is combinedly defined as the net offset. An orientation dependent *net* offset is defined by

$$\Delta(\Omega) = \Delta' + \omega_{iso} + \omega(\Omega), \quad [2]$$

where ω_{iso} is the S-spin isotropic chemical shift. The S-spin rf irradiation is shifted by Δ' relative to ω_{iso}. The I-spin irradiation is assumed to be on-resonance. Employing 2nd rank spherical tensor representation (24, 27), the CSA and dipolar coupling tensors can be written as $\omega(\Omega) \equiv \omega_0^{S,L}$ and $d(\Omega) \equiv \omega_0^{IS,L}$ respectively. The superscripts S and IS denote the CSA and heteronuclear dipolar interactions respectively while L denotes the laboratory frame (z-axis is along the external magnetic field $\mathbf{B}_0$). Euler angles, $\Omega = (\alpha, \beta, 0)$, specify the orientation of the molecular frame, M, with respect to $\mathbf{B}_0$. The components of CSA and heteronuclear dipolar interactions in the laboratory frame are related to their respective principal axis system (PAS or frame P) via the common molecular frame (frame M) by the expression

$$\omega_0^{\chi,L} = \sum_{m=-2}^{2} \mathbf{D}_{m0}^{(2)}(\Omega) \sum_{p=-2}^{2} \omega_p^{\chi,P} \mathbf{D}_{pm}^{(2)}(\Omega_{PM}^\chi), \quad \chi = S, IS, \quad [3]$$

where $\mathbf{D}^{(2)}$ is the 2nd rank Wigner rotation matrix whose elements are functions of the appropriate set of Euler angles (24). Ω_{PM}^χ specifies the orientation of the PAS under consideration in frame M. Figure 2 illustrates these coordinate transformations.

The PAS components of the dipolar interaction are $\omega_m^{IS,P} = \delta_{m0}d_p$ with the $d_p = \gamma_I\gamma_S r^{-3}$, which is the dipolar coupling between I and S nuclei separated by a distance r with the gyromagnetic ratios γ_I and γ_S respectively. The CSA interaction in its PAS is given by the following set of three equations:

$$\omega_0^{S,P} = \omega_0 \Delta\sigma$$
$$\omega_{\pm1}^{S,P} = 0 \quad [4]$$
$$\omega_{\pm2}^{S,P} = \omega_0 \eta \Delta\sigma/\sqrt{6}.$$

The CSA tensor is defined by the anisotropy, $\Delta\sigma = \sigma_{33} - \sigma_{iso}$, and the asymmetry parameter, $\eta = \sigma_{22} - \sigma_{11}/\Delta\sigma$; the magnitudes of the principal elements of the CSA tensor are arranged in the order $\sigma_{11} \leq \sigma_{22} \leq \sigma_{33}$. The isotropic chemical shift is given by $\omega_{iso} = -\gamma_s B_0 \sigma_{iso}$.
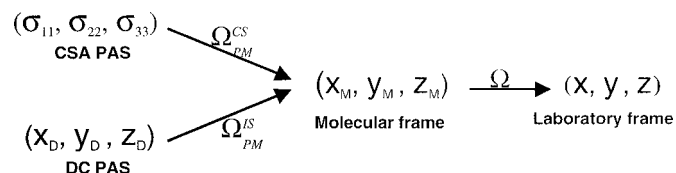
FIG. 2. Reference frame transformations concerned with the spatial part of the CP Hamiltonian and involved in the calculation of the evolution operator $U(t; \phi_I, \phi_S; \Omega)$ for a heteronuclear I–S spin-pair (see Eq. (3) in text). Ω_{PM}^{CS} represents the three Euler angles, $(\alpha_{PM}^{CS}, \beta_{PM}^{CS}, \gamma_{PM}^{CS})$, that transform the PAS of the S-spin chemical shift interaction to frame M. Similarly, Ω_{PM}^{IS} represents Euler angles $(\alpha_{PM}^{IS}, \beta_{PM}^{IS}, \gamma_{PM}^{IS})$ for the transformation from the I–S dipolar interaction PAS to frame M. Ω facilitates transformation from frame M to the laboratory frame.

Time evolution of the density matrix during CP, ignoring relaxation effects for simplicity, is governed by the equation

$$\sigma(t; \phi_I, \phi_S; \Omega) = \mathbf{U}(t; \phi_I, \phi_S; \Omega) \sigma(0) \mathbf{U}^\dagger(t; \phi_I, \phi_S; \Omega), \quad [5]$$

where $\sigma(0)$ is the density matrix prior to the start of CP period. The evolution operator $\mathbf{U}(t; \phi_I, \phi_S; \Omega)$, determined by the Hamiltonian, $\boldsymbol{H}$ (defined in Eq. (1)), is given by

$$\mathbf{U}(t; \phi_I, \phi_S; \Omega) = \mathbf{R_Z}(\phi_I, \phi_S) \mathbf{U}(t; \Omega) \mathbf{R}_z^\dagger(\phi_I, \phi_S) \quad [6a]$$

where

$$\mathbf{R_Z}(\phi_I, \phi_S) = \exp\{-i(\phi_I \mathbf{I_Z} + \phi_S \mathbf{S_Z})\} \quad [6b]$$

and $\mathbf{R}_z^\dagger(\phi_I, \phi_S)$ is its adjoint. Explicit dependence of the matrix elements of the evolution operator on the phases of the CP irradiation rf fields can be given as

$$\mathbf{U}_{kl}(t; \phi_I, \phi_S; \Omega) = \mathbf{U}_{kl}(t; \Omega) \exp\left[-i\left\{\phi_I\left(m_I^{(k)} - m_I^{(l)}\right) + \phi_S\left(m_S^{(k)} - m_S^{(l)}\right)\right\}\right], \quad [7]$$

where $m_I^{(1)} = m_I^{(2)} = m_S^{(1)} = m_S^{(3)}$ is $1/2$ and $m_I^{(3)} = m_I^{(4)} = m_S^{(4)} = m_S^{(2)}$ is $-1/2$, with $m_I^{(k)}$ and $m_S^{(k)}$ denoting the eigenvalues of $\mathbf{I_Z}$ and $\mathbf{S_Z}$ respectively. Together with Eq. [7], the complete evolution operator is determined by

$$\mathbf{U}(t; \Omega) = \mathbf{R}^\mathrm{T} \mathbf{D}(t) \mathbf{R}, \quad \Delta(\Omega) \neq 0, \ d(\Omega) \neq 0, \quad [8]$$

where $\mathbf{R}^\mathrm{T}$ is the transpose and an inverse of $\mathbf{R}$ matrix. For the case with the net offset $\Delta(\Omega) = 0$, $\mathbf{U}(t; \Omega)$ is available in Ref. (26). Elements of the $\mathbf{D}(t)$ matrix are given by

$$D_{kl} = \delta_{kl} e^{-i\lambda_k t}; \quad k, l = 1, 2, 3, 4. \quad [9]$$

λ_k^2 are real and non-negative and the explicit expressions are given by the equations

$$\lambda_1^2(\Omega) = \lambda_4^2(\Omega) = (A + B)/2$$
$$\lambda_2^2(\Omega) = \lambda_3^2(\Omega) = (A - B)/2, \quad [10]$$

with $\lambda_4 = -\lambda_1$ and $\lambda_3 = -\lambda_2$. Explicit expressions for A and B in Eq. (10) are

$$A = a^2 + b^2 + \Delta^2(\Omega) + d^2(\Omega);$$
$$B = 2\sqrt{a^2(b^2 + \Delta^2(\Omega)) + d^2(\Omega)\Delta^2(\Omega)}. \quad [11]$$

The elements of the $\mathbf{R}$ matrix in Eq. [8] which depend on the

parameters a, b, $\Delta(\Omega)$, and $d(\Omega)$ are given by the equation

$$R_{kl} = R'_{kl} \bigg/ \sum_{q=1}^{4} R'^2_{kq}, \quad [12]$$

where $k = 1, 2, 3, 4$ and $l = 1, 2, 3, 4$. For the case of $l = 1$, the matrix elements R'_{kl} is 1 for all values of k, that is $k = 1, 2, 3, 4$. There are three distinct cases for which R'_{kl} with $k = 2$ & 3 are different, while R'_{kl} with $k = 1$ & 4 are the same for all these cases as given below.

Case 1

The matrix elements of the $\mathbf{R}$ matrix in Eq. [12] are given below for the following conditions: (1) nonvanishing dipolar coupling ($d(\Omega) \neq 0$) and net offset ($\Delta(\Omega) \neq 0$), (2) when $k = 1, 4$, and (3) when $k = 2, 3$ if and only if $\lambda_k \neq -d(\Omega)/2$, $\lambda_k \neq 0$.

$$R'_{k2} = (h_{k1}h_{k3} + b^2 - a^2)/[2(d + 2\lambda_k)],$$
$$R'_{k3} = (bh_{k2}R'_{k2} + b^2 - a^2)/ah_{k3}, \quad [13]$$
$$R'_{k4} = [b(a^2 - b^2) - (a^2h_{k3} + b^2h_{k2})R'_{k2}]/ah_{k3}h_{k4}.$$

In Eq. [13], the h_{kl} are given by the following set of equations:

$$h_{k1} = +\Delta(\Omega) + d(\Omega) - 2\lambda_k(\Omega),$$
$$h_{k2} = -\Delta(\Omega) - d(\Omega) - 2\lambda_k(\Omega),$$
$$h_{k3} = +\Delta(\Omega) - d(\Omega) - 2\lambda_k(\Omega), \quad [14]$$
$$h_{k4} = -\Delta(\Omega) + d(\Omega) - 2\lambda_k(\Omega).$$

Case 2

For $k = 2$ or 3, iff $\lambda_k = -d(\Omega)/2 \neq 0$, the matrix elements of $\mathbf{R}$ are given by the following set of three equations:

$$R'_{k2} = 4bd/[a^2 - b^2 + \Delta(2d - \Delta)],$$
$$R'_{k3} = -(2d + \Delta + bR'_{k2})/a, \quad [15]$$
$$R'_{k4} = (\Delta R'_{k2} - b)/a.$$

Note that if $\lambda_2 = -d/2$, then $\lambda_3 = d/2$ and *vice versa*.

Case 3

For $k = 2, 3$, when $\lambda_k = 0$ and $d(\Omega) \neq 0$, the matrix elements of $\mathbf{R}$ are given by the following set of four equations:

$$R'_{22} = -(a^2 - b^2 - \Delta^2 + d^2)/2bd,$$
$$R'_{32} = -1/R'_{22},$$
$$R'_{k3} = -(\Delta + d + bR'_{k2})/a, \quad [16]$$
$$R'_{k4} = [(\Delta + d)R'_{k2} - b]/a.$$

Thus, Eqs. [8]–[16] provide $U(t; \Omega)$ when an offset is present for a nonvanishing dipolar coupling value.

When $d(\Omega) = 0$, the evolution operator $U(t; \Omega)$ in Eq. [7] is given by

$$U(t; \Omega) = \begin{bmatrix} U_{11} & U_{12} & U_{13} & U_{14} \\ U_{12} & U_{11}^* & U_{14} & -U_{13}^* \\ U_{13} & U_{14} & U_{11} & U_{12} \\ U_{14} & -U_{13}^* & U_{12} & -U_{11}^* \end{bmatrix} \qquad [17]$$

with the matrix elements given by the set of equations

$$
\begin{aligned}
U_{11} &= \cos(at/2)[\cos(\omega_e t/2) - i\sin(\omega_e t/2)\cos(\Delta/\omega_e)], \\
U_{12} &= -i\cos(at/2)\sin(\omega_e t/2)\sin(b/\omega_e), \\
U_{13} &= -\sin(at/2)[\sin(\omega_e t/2)\cos(\Delta/\omega_e) + i\cos(\omega_e t/2)], \\
U_{14} &= -\sin(at/2)\sin(\omega_e t/2)\sin(b/\omega_e)
\end{aligned}
\qquad [18]
$$

and the effective field on the S-spin channel, ω_e, is $\sqrt{b^2 + \Delta^2(\Omega)}$. Similarly to the case when $\Delta\Omega = 0$ (26), just four elements of the top row carry all the information regarding evolution of the spin system and all other elements of the $U(t; \Omega)$ matrix are related to these four elements.

The evolution operator $U(t; \Omega)$ described by Eqs. [8]–[18], along with its dependence on rf phases as given by Eq. [7] and the one given in Ref. (26) for the case of $\Delta\Omega = 0$, helps to evaluate the evolution of the spin system for an arbitrary initial condition using Eqs. [4] and [5] under various conditions of rf mismatch, chemical shift anisotropy, and rf offset on S-spin. The expectation value of an operator $\mathbf{A}$, $\langle \mathbf{A} \rangle$, is given by

$$\langle A(t; \phi_I, \phi_S; \Omega) \rangle = \sum_{k=1}^{4} \langle k | A^\dagger \sigma(t; \phi_I, \phi_S; \Omega) | k \rangle. \qquad [19]$$

The density matrix, $\sigma(t; \phi_I, \phi_S; \Omega)$, in the above equation can be written as a linear combination of 16 product operators (25), which can be classified into different (quantum) coherence (QC) orders. As in previous work (26), we elect to use these product operators to track the evolution of the spin system except for pure 0QCs and 2QCs for which $\text{Re}(\sigma_{23})$ (real part of σ_{23}), $\text{Im}(\sigma_{23})$(imaginary part of σ_{23}), $\text{Re}(\sigma_{14})$, and $\text{Im}(\sigma_{14})$ are monitored. For a distribution of molecular orientations the sum of contributions to the expectation value from all orientations weighted by the orientation distribution function, $p(\Omega)$, is given by

$$\langle\langle A(t; \phi_I, \phi_S) \rangle\rangle = \int d\Omega \, p(\Omega)\langle A(t; \phi_I, \phi_S; \Omega) \rangle \qquad [20]$$

where $d\Omega = d\alpha \, d\beta \sin\beta$, $0 \le \alpha \le 2\pi$, and $0 \le \beta \le \pi$. For a powder sample, the distribution function, $p(\Omega)$, is $\frac{1}{4\pi}$.

3. EXPERIMENTAL

A powder sample of N-acetyl-^{15}N-D,L-valine (NAV) and a single crystal of N-acetyl-^{15}N-L-valyl-^{15}N-L-leucine (NAVL) were used in solid-state NMR experiments to investigate the effects of an offset, HH-mismatch during CP and the post-CP pulse on ^{15}N-spin. Preparation of NAV and NAVL samples is given elsewhere (28). All spectra were acquired on a Chemagnetics/ Varian Infinity-400 spectrometer, using a double resonance Chemagnetics magic angle spinning (MAS) probe, operating at 400.139 MHz (9.4 T) for ^{1}H and 40.551 MHz for ^{15}N. A spectral width of 100 kHz and a recycle delay of 5 s were used. Typical pulse lengths for a $\frac{\pi}{2}$ flip angle were 3.25 μs and 4.4 μs for ^{1}H and ^{15}N spins respectively. Static ^{15}N chemical shift powder spectra were collected using the spin echo sequence $\tau - \pi - \tau$ (21). The spin echo delay employed was $\tau = 60$ μs. During signal acquisition protons were decoupled from ^{15}N spins with a decoupling rf power of 77 kHz using the TPPM decoupling pulse sequence. The ^{15}N rf carrier frequency was switched to its offset value before the CP period and switched back to coincide with its isotropic chemical shift after CP so that the post-CP pulse and refocusing π pulse (for static powder experiments) were applied on resonance. Typically 400 ns were sufficient to carry out the frequency jump during the pulse sequence. For the NAV powder sample, 560 transients were accumulated each with 256 data points under static condition and 16 transients were accumulated each with 4096 data points under magic angle spinning. For the NAVL single crystal about 128 transients were accumulated using about 512 data points. All data were zero filled to a total of 4096 complex points prior to Fourier transformation. Other details can be found in figure captions.

4. RESULTS AND DISCUSSION

Simulations of the evolution of coherences under various CP conditions are given in Figs. 3 to 9. We assume that the S-spin CSA in PAS is given by $\Delta\sigma = -4.265$ kHz and $\eta = 0.29$, which correspond to the ^{15}N CSA tensor of [^{15}N-Gly-18]magainin2 peptide (the corresponding Cartesian principal components of the shielding tensor are 42.3, 72.7, and 215.3 ppm) at 400 MHz ^{1}H resonance frequency (29). We also assume $d_P = -11.2$ kHz that corresponds to the ^{1}H–^{15}N dipolar coupling constant for the same amide ^{15}N site of the magainin2 peptide. The relative orientation of the PAS of the CSA and dipolar coupling tensors is given by the Euler angles (30, 22, 0). We assume the I-spin rf irradiation is on-resonance and the strength, a, is 30 kHz.

Figure 3 shows the evolution of coherences during CP under perfect HH-match condition at a molecular orientation $\Omega = (0, -22, 0)$. The S-spin rf is applied on resonance ($\Delta' = 0$); hence only the CSA contributes to the offset resulting in $\Delta = -3.4$ kHz. Figure 3a shows the evolution of ± 1QCs. When compared with the evolution under $\Delta = 0$ (Fig. 1(a) of Ref. 26), it shows that there is a small but unmistakable presence of $\mathbf{S}_y$ whereas $\mathbf{I}_y$ is still zero. Similarly, Fig. 3b reveals the generation
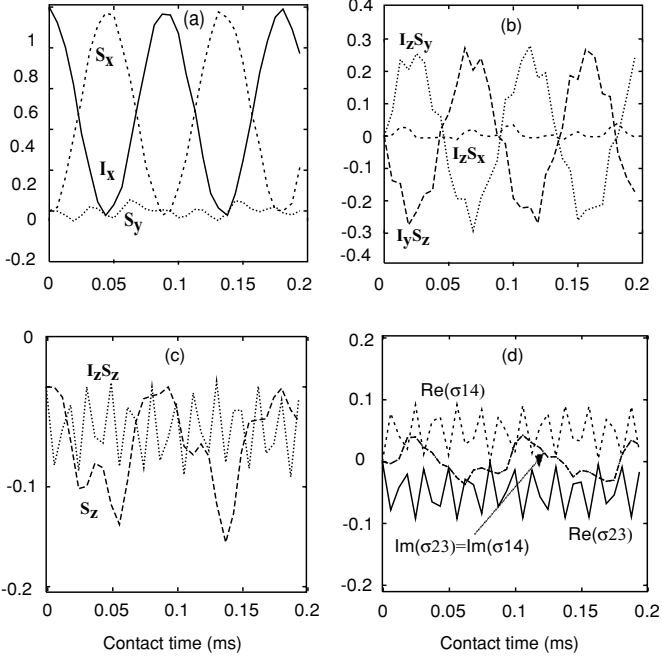
FIG. 3. Time evolution of coherences during HH-match CP for a heteronuclear spin-$\frac{1}{2}$ pair with the S-spin rf irradiation on-resonance, $\Delta' = 0$ (in this work I-spin irradiation is assumed to be always on-resonance). The S-spin chemical shift $\omega(\Omega)$ imparts an orientation dependence to the net offset $\Delta = \Delta' + \omega$. I and S-spin rf field strengths are assumed to be 30 kHz. $\Delta\sigma$ and η describing the CSA components in CSA PAS are respectively -4.265 kHz and 0.29. Dipolar coupling, in its DC PAS $d_P = -11.2$ kHz. Euler angles describing the I–S dipole coupling vector orientation relative to the CSA tensor are (30, 22, 0). The relative orientation of the magnetic field $\mathbf{B}_0$ and the molecular frame M is given by $\Omega = (-30, -22, 0)$, yielding $d_P = -11.2$ kHz, $\Delta = \omega = -3.4$ kHz. (a) $\pm$1QCs, $\mathbf{I}_y = 0$, (b) antiphase $\pm$1QCs, $\mathbf{I}_x\mathbf{S}_z = 0$, (c) $\mathbf{I}_z = 0$, $\mathbf{S}_z$ and longitudinal order $\mathbf{I}_z\mathbf{S}_z$, (d) pure 0QCs and $\pm$2QCs. The small but unmistakable presence of $\mathbf{S}_y$ (in (a)) as well as those of $\mathbf{I}_z\mathbf{S}_x$ (in (b)) and $\mathbf{S}_z$ (in (c)) indicates the introduction of offset into CP dynamics (compare with similar plots in Figs. 1 and 2 in Reference (26)). See text for more information.

of nonzero $\mathbf{I}_z\mathbf{S}_x$ and Fig. 3c that of $\mathbf{S}_z$ (compare Figs. 3b and 3c with Fig. 1c and Fig. 2a of Ref. 26, respectively). Differences in the evolution of pure 0QCs and 2QCs (see Fig. 3d) can be discerned when compared to the corresponding evolutions with $\Delta = 0$ (26). Powder averages of these plots (not shown) are similar to those under the condition of $\Delta = 0$ (26).

The effect of changing the molecular orientation, relative to the laboratory frame, from the one in Fig. 3 to an orientation defined by $\Omega = (0, 54.74, 0)$ (resulting in $d_P = 4.4$ kHz and $\Delta = \omega = -0.4$ kHz) is shown in Figs. 4a–4d. The presence of a small value of Δ leads to a large change in the amplitudes of all coherences except $\mathbf{I}_x$ and $\mathbf{S}_x$ (see Figs. 4a–4d). The dipolar coupling used in Figs. 4a–4d is less than half of that in Fig. 3 and therefore the rates of evolution of coherences are slowed down (see Figs. 3a and 3b). Since the CSA is much smaller compared to a, b, and d_p (terms are defined in Eq. [1]), it turns out that the molecular orientation Ω does not have a significant influence on the amplitudes of magnetization exchange as indicated

by the time courses of $\mathbf{I}_x$ and $\mathbf{S}_x$ (see Fig. 4a), though the rates are influenced by Ω via its effect on $d(\Omega)$. We will return to the issue of the influence of the relative orientation of CSA and dipolar interaction on the evolution of coherences later in the discussion.

The effect of a large rf offset on the evolution of various coherences during CP is shown in Figs. 4e–4h. An rf offset, Δ', of -15 kHz results in a net offset, Δ, of -15.4 kHz. The rest of the parameters are the same as in Figs. 4a–4d. As expected, due to the tilted effective rf field on the S-spin, the increase in the expectation value of $\mathbf{S}_z$ is significant (see Fig. 4g). Note substantial increases in one of the antiphase magnetizations, namely $\mathbf{I}_z\mathbf{S}_x$ (compare Figs. 4f and 3b), $\mathbf{I}_z\mathbf{S}_z$ (given in Fig. 4g), and the pure 0QC and 2QCs given in Fig. 4h, when compared to Figs. 3 and 4a–4d. Also note that the exchange among $\mathbf{I}_x$ and $\mathbf{S}_x$ is slower (see Fig. 4e) compared even to that in Fig. 4a and $\mathbf{S}_y$ reappears (see Fig. 4e). Thus the large rf offset is able to generate coherence modes that are normally absent when the Hamiltonian and the evolution are confined to 0QC and 2QC subspaces, and also slows down the exchange of $\pm$1QCs between the spins.

Since the effective rf field during CP is tilted due to the presence of an offset on the S-spin channel, the transferred magnetization from I-spin to S-spin is polarized along the effective field axis. Therefore, in order to generate a maximum transverse S-spin magnetization, a post-CP pulse is used to tilt the magnetization from the tilted plane to the xy plane (see the pulse sequence given in Fig. 1). Figure 5 shows the result of post-CP manipulation by an S-spin pulse whose flip angle and phase are adjusted to compensate the offset generated tilt of the effective field. All the other parameters are the same as given in Figs. 4e–4h. Comparison of the respective panels in these two figures (Figs. 4e–4h and 5) shows that $\mathbf{S}_x$ evolution is "smoothed" by the post-CP pulse and the rest of the $\pm$1QCs are unaltered. The post-CP pulse also reduces $\mathbf{S}_z$ greatly but the $\mathbf{I}_z\mathbf{S}_z$ is not changed significantly and $\mathbf{I}_z = 0$ is unchanged. The imaginary parts of pure 0QC and 2QCs are reduced while the amplitudes of the real parts of these coherences are unaltered (compare Figs. 4d, 4h, and 5d).

Figures 6a–6d attempt to identify qualitative similarities between the effects of a large offset and a comparable HH-mismatch during CP, when these conditions exist independently. Here, $a = 30$ kHz, $b = 25.75$ kHz, and all other parameters are the same as in Figs. 4a–4d. Comparing with Fig. 3, it can be seen that HH-mismatch also slows down the exchange between $\mathbf{I}_x$ and $\mathbf{S}_x$ (see Fig. 6a), but unlike the large offset case, no $\mathbf{S}_y$ is generated and only a miniscule amount of $\mathbf{S}_z$ (Fig. 6c) is produced due to the CSA (compare with similar plots for the HH-match condition given in the reference 26). $\mathbf{I}_x\mathbf{S}_z$ is not generated, but large amounts of $\mathbf{I}_z\mathbf{S}_z$ (see Fig. 6c) and real parts of 0QC and 2QC (see Fig. 6d) are generated. There are no "ripples" in the trajectory of $\mathbf{S}_x$ as witnessed in the case of a large offset.

Figures 6e–6h depict an effort to compensate for the mismatch condition in Figs. 6a–6d by introducing S-spin rf offset $\Delta = -15$ kHz. It is instructive to compare the corresponding panels of Figs. 4e–4h and 6a–6h. Now, the effective field on both
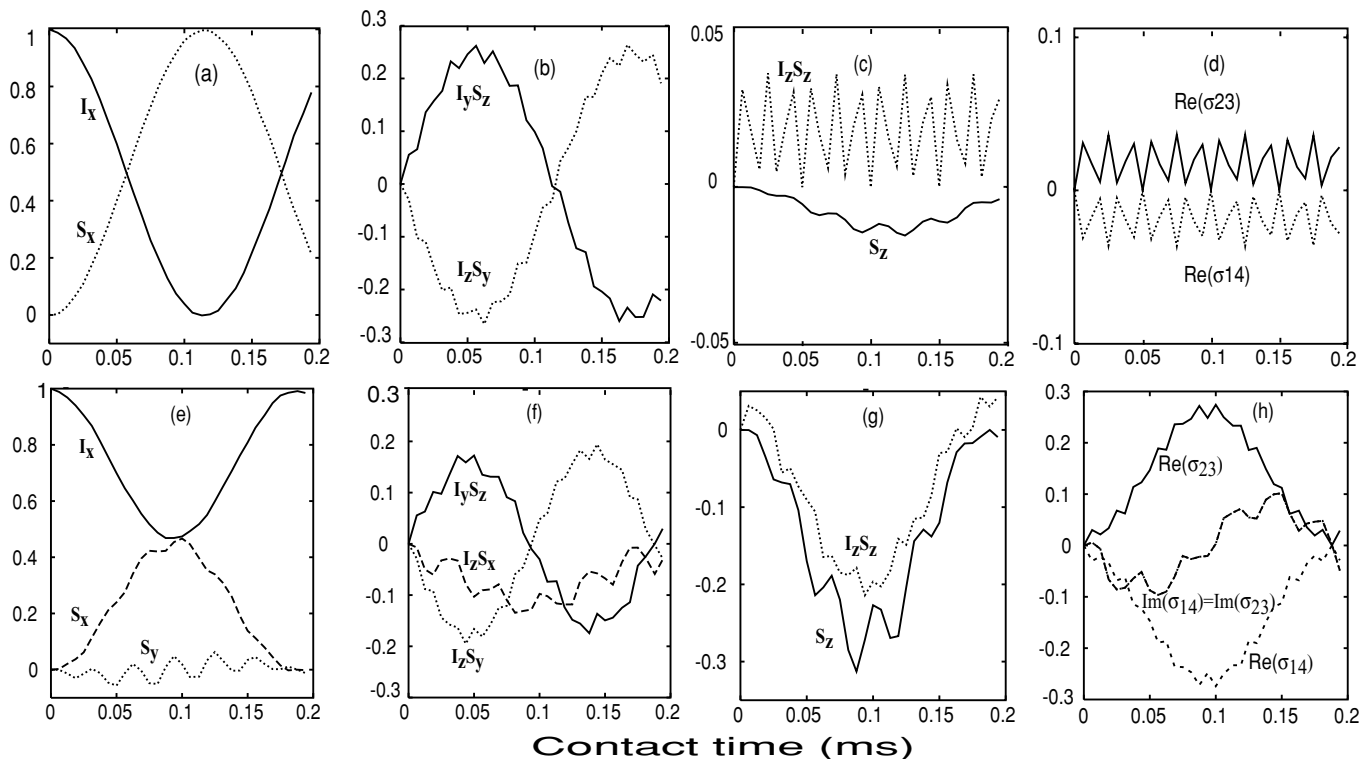
FIG. 4. Simulations describing the effect of the molecular frame, M, orientation (a–d) and an rf offet of -15.4 kHz (e–h) on the evolution of coherences during CP. A molecular frame orientation defined by $\Omega = (0, 54.7355, 0)$ is assumed and this resulted in $d = 4.4$ kHz and $\Delta = \omega = -0.4$ kHz. All other parameters are the same as in Fig. 3. (a) $\pm$1QCs, $\mathbf{I}_y = \mathbf{S}_y = 0$, (b) antiphase $\pm$1QCs, $\mathbf{I}_x\mathbf{S}_z = \mathbf{I}_z\mathbf{S}_x = 0$, (c) longitudinal order $\mathbf{I}_z\mathbf{S}_z$, $\mathbf{I}_z = 0$, $\mathbf{S}_z$, (d) pure 0QCs and $\pm$2QCs with nearly zero imaginary parts, (e) $\pm$1QCs, $\mathbf{I}_y = 0$, (f) antiphase $\pm$1QCs, $\mathbf{I}_x\mathbf{S}_z = 0$, (g) longitudinal order $\mathbf{I}_z\mathbf{S}_z$, $\mathbf{I}_z = 0$, $\mathbf{S}_z$, and (h) pure 0QCs and pure $\pm$2QCs. See Fig. 3 caption and text for more information on the parameters.

I- and S-spin channels is the same, $\sqrt{b^2 + \Delta'^2} = a = 30$ kHz. The maximum $\mathbf{S}_x$ is considerably boosted up to 85% and the signature ripples due to the large offset can be seen in Fig. 6e. Though one can expect the amplitude of $\mathbf{S}_z$ to increase, it is nearly twice as much as the amplitude in Figs. 4e–4h (i.e., with the offset alone and without the HH-mismatch) and $\mathbf{I}_z\mathbf{S}_z$ is reduced to a large extent, as well as $\mathbf{I}_z\mathbf{S}_x$ (see Fig. 6f) and pure 0QC and $\pm$2QCs (see Fig. 6h). One can also note that the amplitude of $\mathbf{S}_x$ in Fig. 6e is greater than in Fig. 5a, though with the above-mentioned ripples. The rate of exchange here is somewhat slower than the case of either the offset (see Figs. 4e–4h) or HH-mismatch (see Figs. 6a–6d) alone.

The amplitude of $\mathbf{S}_x$ can be recovered fully even in the presence of a large offset by compensating for both HH-mismatch and the tilt of the effective field on S-spin as demonstrated in Figs. 6i–6l. Here, as in Figs. 6e–6h, the effective field on both channels is 30 kHz but the CP is immediately followed by an S-spin post-CP pulse (see Fig. 1). Restoration of $\mathbf{S}_x$ to its maximum possible amplitude is complete; the presence of a large offset is hinted at by the small but persistent presence of $\mathbf{S}_y$. The rest of the coherence modes more or less approach the behavior under the perfect HH-match (compare with Figs. 4a–4d for parameters to the ones in Figs. 6i–6l). An important feature is that

the rate of exchange among $\mathbf{I}_x$ and $\mathbf{S}_x$ is considerably slower in Fig. 6i than under the perfect HH-match without an offset. This can be attributed to the fact that an offset scales the magnitude of the heteronuclear dipolar interaction (*30*) during CP.

Now we turn our attention to powder averages (*31, 32*) of the situations discussed above. We examine the influence of the relative orientation of the CSA and dipolar interactions defined by Ω_{PM} on the CP dynamics. Figure 7 illustrates the effect of two sets of random molecular orientations for two different sets of Euler angles Ω_{PM}. Figures 7a and 7b correspond to the same relative orientation, $\Omega_{PM} = (0, 22, 30)$, while 7c and 7d correspond to another relative orientation, $\Omega_{PM} = (0, 0, 0)$. Figures 7a and 7c are the result of superposition of $\pm$1QCs from the same set of five random molecular orientations defined by Ω. Similarly Figures 7b and 7d correspond to the same set of 25 random molecular orientations. It is clear that for both of these small sets of random molecular orientations the superposed time courses are of different patterns for different Ω_{PM} (compare Figs. 7a with 7c and Figs. 7b with 7d). But these differences disappear when a large number ($\geq$1000) of random molecular orientations are considered, i.e., when a full powder average is conducted, as revealed in Fig. 8. Figures 8a and 8c correspond to two different Ω_{PM}, given in Figs. 7a and 7b, respectively. Thus, for the
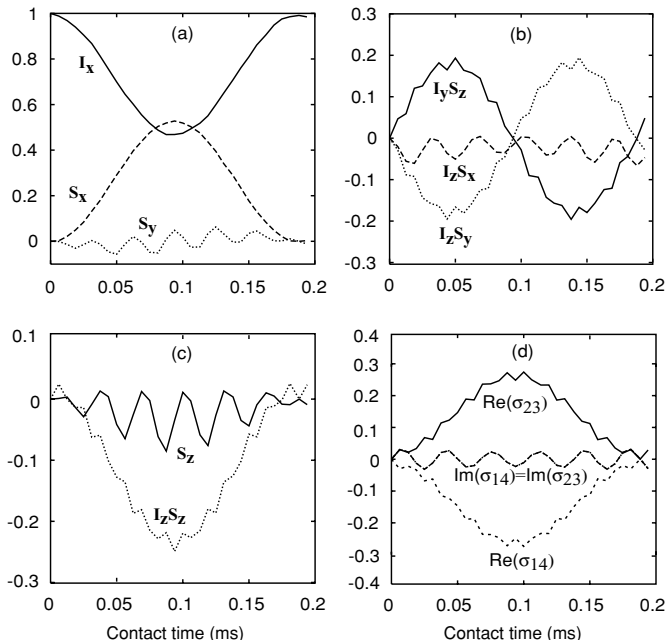
FIG. 5. Simulations describing the effect of an S-spin post-CP pulse with a flip angle $\theta = -31°$ and $\phi_S = \pi/2$ compensating for the tilt (due to offset) of the effective field on the evolution of coherences during CP. All other parameters are same as given in Fig. 3. (a) ± 1QCs, $\mathbf{I}_y = 0$, (b) antiphase ± 1QCs, $\mathbf{I}_x \mathbf{S}_z = 0$, (c) longitudinal order $\mathbf{I}_z \mathbf{S}_z$, $\mathbf{I}_z = 0$, $\mathbf{S}_z$, (d) pure 0QCs and pure ± 2QCs. See Fig. 3 caption for more information on the parameters.

given CSA and dipolar coupling values, powder averages render the influence of Ω_{PM} ineffective in the evolution of coherences during CP. However, as discussed below, this depends on the magnitudes of CSA and dipolar coupling tensors. For example, the CP dynamics given in Figs. 8b and 8d is different because the CSA is much larger than the dipolar coupling, where the Ω_{PM} is as in Figs. 8a and 8c; differences in time courses persist even with as many as 15,000 random orientations in powder averaging. Thus, in principle the relative orientation of the tensors, Ω_{PM}, is important (especially in high magnetic fields where the CSA span is larger) (*33–35*), though there could be regions of magnitudes of ω and d_P where its effect is minimal (see Figs. 8a and 8c).

Powder averages of $\mathbf{S}_x$ evolution during CP with a large offset (Fig. 9a), offset compensated mismatch (Fig. 9b), and with both HH-mismatch compensation and the resulting tilt compensation with a post-CP pulse (Fig. 9c) are shown in Figs. 9a–9c, demonstrating the efficacy of the double compensation. The bottom, middle, and top curves in Figs. 9a–9c are powder averaged counterparts of $\mathbf{S}_x$ in Figs. 4e, 6e, and 6i respectively. It is clear that the double compensation procedure significantly enhances the sensitivity of the CP experiment.

The dependence of maximum $\mathbf{S}_x$ amplitude as a function of rf offset, Δ', for a single molecular orientation and powder averages under various CP conditions is given in Figs. 9d and 9e. In Fig. 9d, the outer (solid line), middle (dashed line), and

inner curves (dotted line) show the dependence of maximum $\mathbf{S}_x$, attained for the usual HH-match ($a = b$), as a function of Δ' for three different orientations, Ω. The inner curve is almost symmetric about $\Delta' = 0$ and this may be attributed to the small value of chemical shift for molecular orientation $\Omega = (0, 54.7, 0)$. The maxima for the middle and outer curves are shifted to positive values of Δ'. All three curves reach the same maximum value of $\mathbf{S}_x$.

The effect of rf offset during CP on a powder sample is simulated and the results are given in Fig. 9e. The inner curve in Fig. 9e corresponds to powder averages for the curves in Fig. 9d. The middle curve shows the dependence of the powder averaged maximum $\mathbf{S}_x$ amplitude under the condition of $\sqrt{b^2 + \Delta^2}$ as a function of rf offset Δ'. The outer curve is the result of using a post-CP S-spin pulse that compensates the tilt of the effective field existing at each point in the middle curve. It is obvious that the double compensation increases the tolerance of the CP sequence against the rf offset. For example, at an rf offset of 20 kHz, the regular CP sequence transfers $\sim$20%, while the double compensated CP pulse sequence transfers $\sim$56% of the transverse magnetization from I to S nuclei.

The efficacy of the double compensated CP sequence was experimentally examined on single crystal and powder samples of peptides. The results are discussed below. The ^{15}N chemical shift spectra of NAV powder sample are given in Fig. 10. The proton rf field strength, a, was always held at 41.67 kHz in these experiments. The ^{15}N rf carrier was set to coincide with the isotropic peak of NAV at 40.5505 MHz. In Fig. 10a $a = 41.67$ kHz and $b = 20.8$ kHz, while for Fig. 10b $a = 41.67$ kHz and $b = 30$ kHz, thus dealing with two different sets of HH-mismatches and corresponding offsets when the effective fields are brought up to match a. The trend of progressive improvement of the signal to noise ratio (S/N) from the HH-mismatch/large rf offset $\rightarrow$ offset compensated HH-mismatch, i.e., $a = \sqrt{b^2 + \Delta^2} \rightarrow$ double compensation involving post-CP pulse in both cases are shown in Figs. 10a and 10b. A minor detail to notice is that for the smaller mismatch case of Fig. 10b the offset alone spectrum has a poorer S/N compared to the HH-mismatch alone spectrum, while in Fig. 10a the situation is reversed. The improved spectra require an increase in contact time from 1 to 3 ms in accordance with the theoretical predictions and simulations outlined earlier that the introduction of an offset and/or an HH-mismatch tends to slow down the rates of evolution of 1QCs due to the scaling on the magnitude of the ^{1}H–^{15}N dipolar coupling effective during CP. Increasing the contact time further had no improvements in the CP signal; the results were unchanged up to a contact time of 5 ms.

The performance of the pulse sequence under MAS is similar to the static case. The results are displayed in Fig. 11 for spinning rates of 1.5 and 3 kHz. Spectra (a), (b), (c), and (d) respectively correspond to HH-match, HH-mismatch, offset compensated HH-mismatch, and post-CP pulse corrected offset compensated mismatch conditions of Fig. 10a. When the results shown in Figs. 10 and 11 are compared to the curves in Fig. 9e (at say,
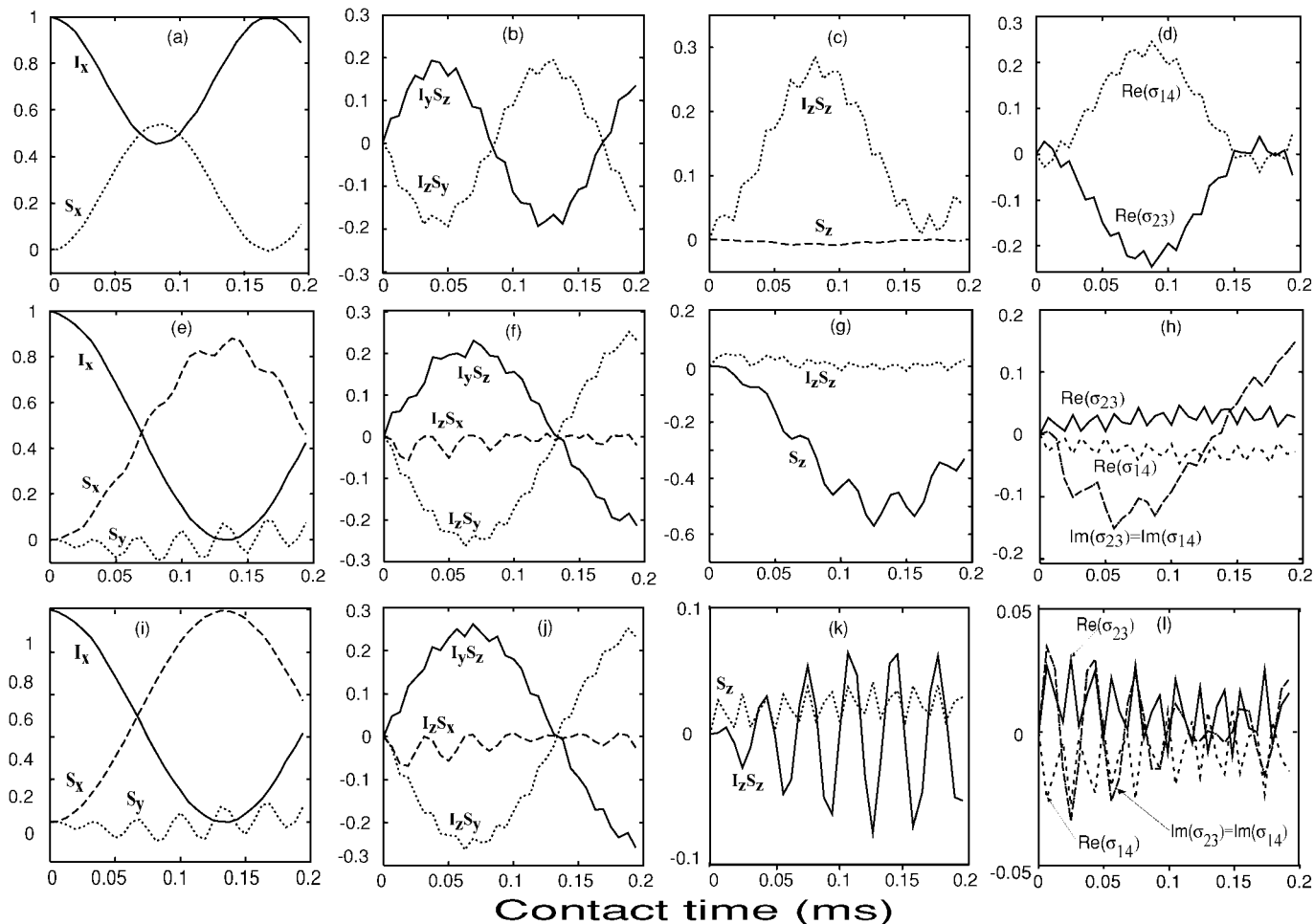
FIG. 6. Simulations illustrating the effect of HH-mismatch of rf field strengths during CP (a–d), the S-spin rf field offset compensated HH-match CP (e–h), and the S-spin offset compensated HH-match CP accompanied by a post-CP pulse (i–l). Rf field strengths of $a = 30$ kHz on the I-spin channel and $b = 25.75$ kHz on the S-spin channel were assumed. An $\Delta' = -15$ kHz was assumed for figures (e–l), and $\theta = -31°$ and $\phi_S = \pi/2$ were used for the post pulse in figures (i–l). All the other parameters are the same as in Fig. 4. (a, e, i) ± 1QCs, $\mathbf{I}_y = 0$, (b, f, j) antiphase ± 1QCs, $\mathbf{I}_x \mathbf{S}_z = 0$, (c, g, k) longitudinal order $\mathbf{I}_z \mathbf{S}_z$, $\mathbf{I}_z = 0$, $\mathbf{S}_z$, (d, h, l) pure 0QCs and ± 2QCs. $\mathbf{S}_y = 0$ in (a), $\mathbf{I}_z \mathbf{S}_x = 0$ in (b), and the imaginary parts are nearly zero in (d). See Fig. 3 caption for additional information.

$\Delta' = 30$ kHz), the agreement between the theoretical predictions and the experimental results is gratifying. Experimental results obtained from a single crystal of the doubly ^{15}N-labeled NAVL dipeptide are presented in Fig. 12. The spectra shown in Figs. 12a and 12b correspond to the same orientation of the crystal relative to the magnetic field and have one-to-one correspondence regarding the CP conditions of Figs. 11a and 11d, respectively. Experiments under the CP conditions of Figs. 11b and 11c produced similar results (not shown). The four peaks in Figs. 12a and 12b arise from four magnetically distinct ^{15}N sites from the two NAVL molecules per unit cell. It can be seen that mismatch compensation by offset is effective once again and that the post-CP pulse enhances the coherence transfer further. However, the HH-match (a) and fully compensated (b) spectra show different relative intensities amongst the peaks though the overall S/N for these spectra is very similar (i.e., the highest peak in each spectrum has the very similar intensity, though they are

not the same peaks in the two spectra). This may be attributed to possible different 1QC trajectories for each of the distinct sites in the single crystal, due to the difference in the ^{1}H–^{15}N dipolar coupling magnitude of different sites, and their modification to different extents for changes in the CP conditions. Such an effect has been utilized in the SPECIFIC CP pulse sequence for spectral simplification or resonance assignment in molecules that are uniformly labeled with ^{15}N and ^{13}C isotopes (9). As in Figs. 10 and 11, under the conditions of offset compensated HH-mismatch, it was necessary to increase the contact time from 1 to 3 ms to obtain the best possible S/N for the spectrum shown in Fig. 12b. Spectra shown in Figs. 12c and 12d are for a different orientation of the crystal relative to the external magnetic field, but under the same CP conditions as in Figs. 12a and 12b. Once again note the differences in the relative intensities within each spectrum and changes in these differences between the spectra. As usual, the S/N is practically restored to its full value when
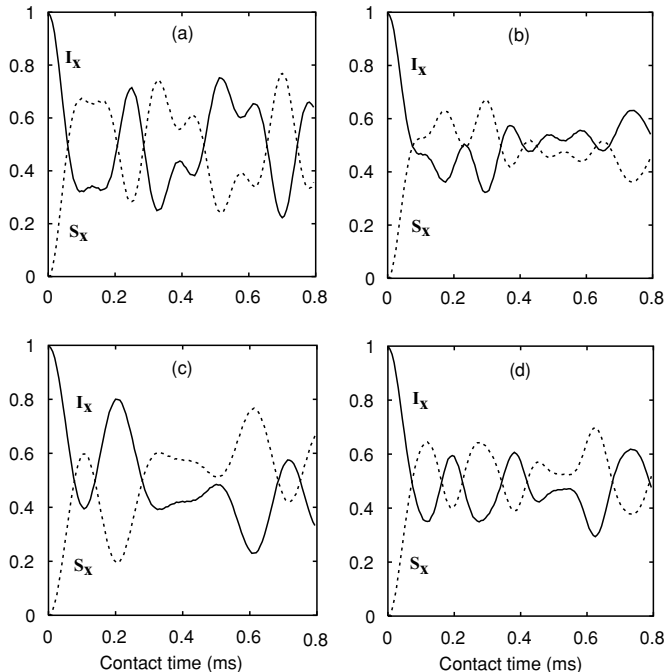
FIG. 7. Effect of number of random molecular orientations defined by the Euler angles (α, β, γ) on the influence of the relative orientation of CSA and dipolar interactions on evolution of ± 1QCs during CP. Values of the parameters used in the simulations are $a = b = 30$ kHz, $\Delta\sigma = -4.265$ kHz, $\eta = 0.29$, $d_p = -11.2$ kHz, $(\alpha_{PM}, \beta_{PM}, \gamma_{PM}) = (0, 22, 30)$ for (a) and (b), and $(\alpha_{PM}, \beta_{PM}, \gamma_{PM}) = (0, 0, 0)$ for (c) and (d). (a) and (c) are obtained for the identical set of 5 random molecular orientations. Figures (b) and (d) are identical set of 25 random molecular orientations.

double compensation is employed but with one crucial difference. One of the peaks present under HH-match disappears when double compensation is employed (see Fig. 12d), only to reappear at some other values of contact times, say 8 ms (spectrum not shown). Spectra were also acquired at contact times ranging from 0.5 ms to 9 ms (not shown). Relative intensities as a function of contact time were found to be different and to some extent oscillate. Experiments were also conducted under the HH condition of Fig. 12c as a function of contact time and oscillatory features were observed (spectra not shown), but the overall S/N were comparable between contact times of 1 and 10 ms. At yet another orientation of the crystal, one of the peaks disappeared for the offset compensated HH-mismatch condition (with $\sqrt{b^2 + \Delta'^2} = a$) without the post-CP pulse for a contact time of 3 ms, but reappeared for a contact time of 5 ms. However, the experiment involving the post-CP pulse for a contact time of 3 ms and with identical remaining conditions consisted of all the peaks. These observations (spectra not shown) are similar and complementary to the results shown in Figs. 12c and 12d.

Thus, the 1QC trajectories differ for different sites during CP, resulting in different relative intensities for magnetically distinct sites, because of different anisotropic magnetic interactions, viz., CSA and dipolar coupling. In addition, these dif-

ferences are modified to different extents (including oscillations and overall slowdown) in the presence of offset and HH-mismatch conditions as well as of post CP manipulations via pulses. It should be noted that the pure oscillations predicted by the theoretical treatment are in practice damped by the relaxation effects and spin diffusion caused by dipolar interactions of one or both of the heteronuclear spin pair with other spins, both of which were ignored from the treatment presented in this study.

Offset assisted rf power reduction in the CP pulse sequence could be valuable for the applications of solid-state NMR experiments (36) on power lossy wet biological samples such as lipid bilayers (37). The theoretical results presented in this paper could be used to design efficient low-power rf pulse sequences for such applications. It should be pointed out that the use of rf offset on the ^{1}H channel may reduce the S/N of CP experiments by scaling down the ^{1}H–^{1}H dipolar interactions (38). Further study dealing with the analysis of the efficiency of variable amplitude CP (39) and other variants of the CP pulse sequence (8, 16, 40), against the effects of offset and HH-mismatch, is in progress in our laboratory. Also, the design of efficient pulse sequences, based on the present work, for indirect detection experiments (41–44) is in progress.
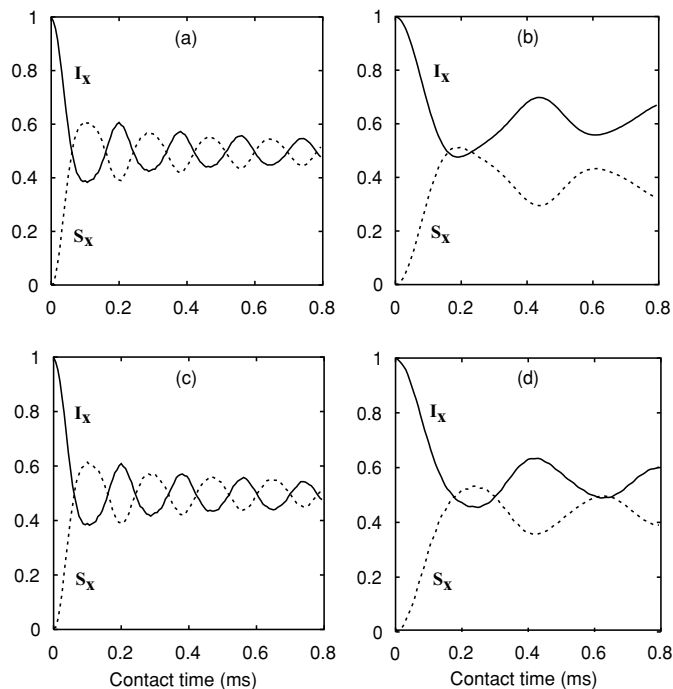
FIG. 8. Calculations showing the influence of magnitudes and relative orientations of CSA and dipolar interaction tensors on evolution of ± 1QCs during CP for a powder. Values of the parameters used in the simulations are $a = b = 30$ kHz, $\Delta' = 0$ and $\eta = 0.29$. (a) and (c) are powder averages of Figs. 8a and 8c, whereas (b) and (d) are powder averages with $\Delta\sigma = -15$ kHz and $d = -5$ kHz. The Euler angles $(\alpha_{PM}, \beta_{PM}, \gamma_{PM})$ used in (b) and (d) are (0, 54.7, 0) and (0, 0, 0), respectively.
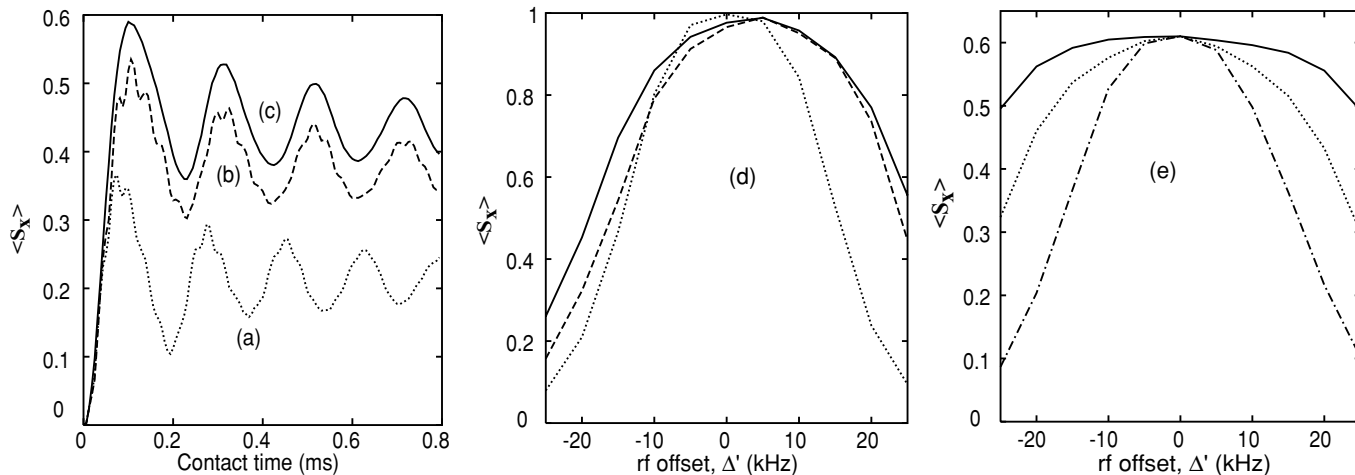
FIG. 9. Powder average of S_x for parameters in Figs. 4e, 6e, and 6i are respectively represented by the bottom (a), middle (b), and top curves (c). (d) Results of calculations illustrating the influence of the orientation of the molecular frame, M, on the maximum amplitude of S_x during CP as a function of rf offset Δ'. Values of the parameters used in the calculations of figure (d) are $a = b = 30$ kHz, $\Delta\sigma = -4.265$ kHz, $\eta = 0.29$, $d_p = -11.2$ kHz and $\Omega_{PM} = (0, 22, 30)$. The outer, middle, and inner curves in (d) correspond to Euler angles $\Omega = (-30, -22, 0)$, $(0, 0, 0)$, $(0, 54.7, 0)$ respectively, yielding $\omega = -3.4, -4.3$, and -0.4 kHz and $d = -11.2, -8.8$, and -4.4 kHz. (e) The powder averaged maximum amplitude of S_x during CP for the conditions of no mismatch compensation (inner curve), offset compensated HH-match (middle curve), and offset as well as tilt compensated (by S-spin post-CP pulse) HH-match (outer curve).
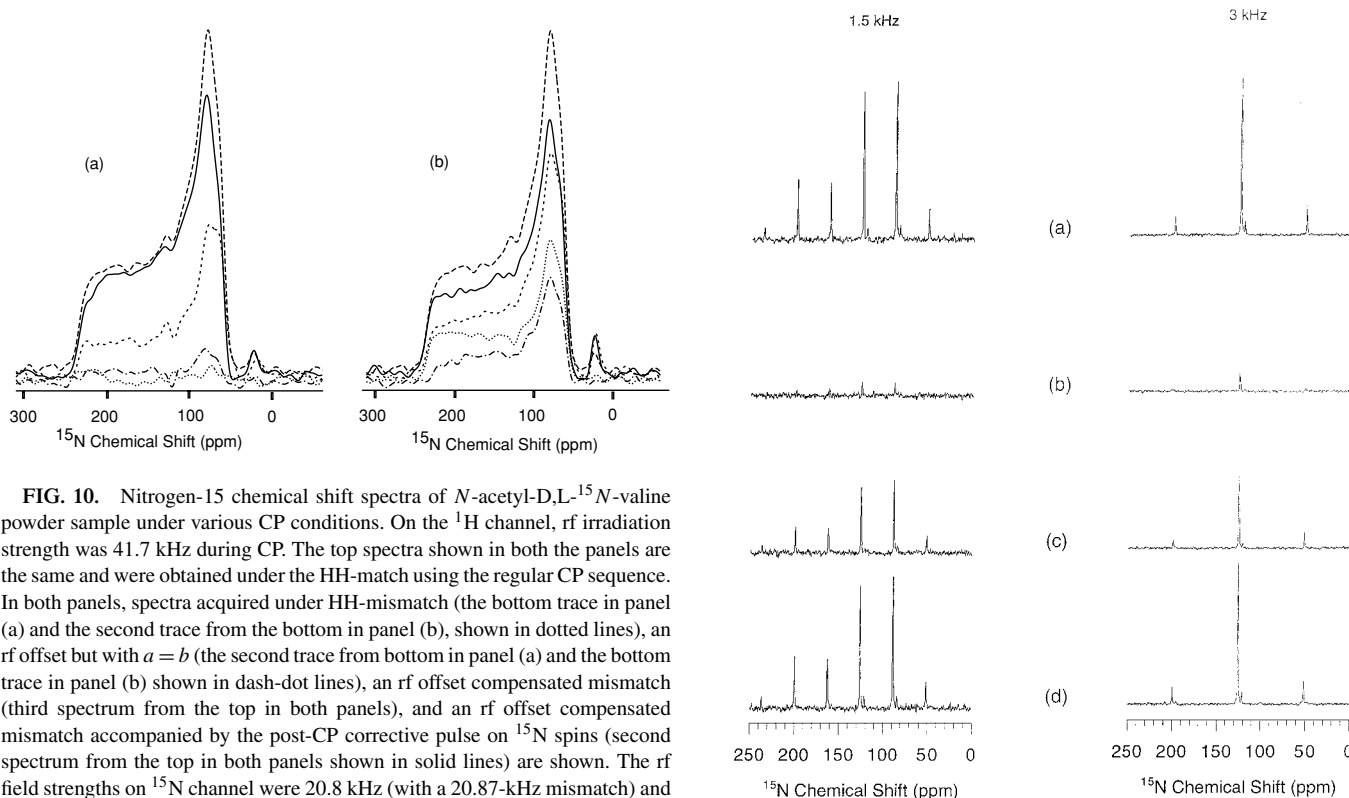
FIG. 10. Nitrogen-15 chemical shift spectra of N-acetyl-D,L-^{15}N-valine powder sample under various CP conditions. On the ^{1}H channel, rf irradiation strength was 41.7 kHz during CP. The top spectra shown in both the panels are the same and were obtained under the HH-match using the regular CP sequence. In both panels, spectra acquired under HH-mismatch (the bottom trace in panel (a) and the second trace from the bottom in panel (b), shown in dotted lines), an rf offset but with $a = b$ (the second trace from bottom in panel (a) and the bottom trace in panel (b) shown in dash-dot lines), an rf offset compensated mismatch (third spectrum from the top in both panels), and an rf offset compensated mismatch accompanied by the post-CP corrective pulse on ^{15}N spins (second spectrum from the top in both panels shown in solid lines) are shown. The rf field strengths on ^{15}N channel were 20.8 kHz (with a 20.87-kHz mismatch) and 30 kHz (with a 11.67-kHz mismatch) for panels (a) and (b) respectively. The rf offsets used to satisfy $a = \sqrt{b^2 + \Delta^2}$ were 36.1 and 28.9 kHz, while the flip angles of the post-CP pulses were 60° and 40° in panels (a) and (b) respectively. From bottom to top, areas of the spectra in panel (a) are 0.01, 0.04, 0.43, 0.86, and 1, while for panel (b) they are 0.23, 0.39, 0.64, 0.79, and 1. A slowdown of CP dynamics in the presence of HH-mismatch and/or offset required an increase of contact time from 1 ms to 3 ms for the optimal performance of pulse sequence of Fig. 1 (see subsequent figures for more results on this aspect). See Fig. 1 and text for more information.
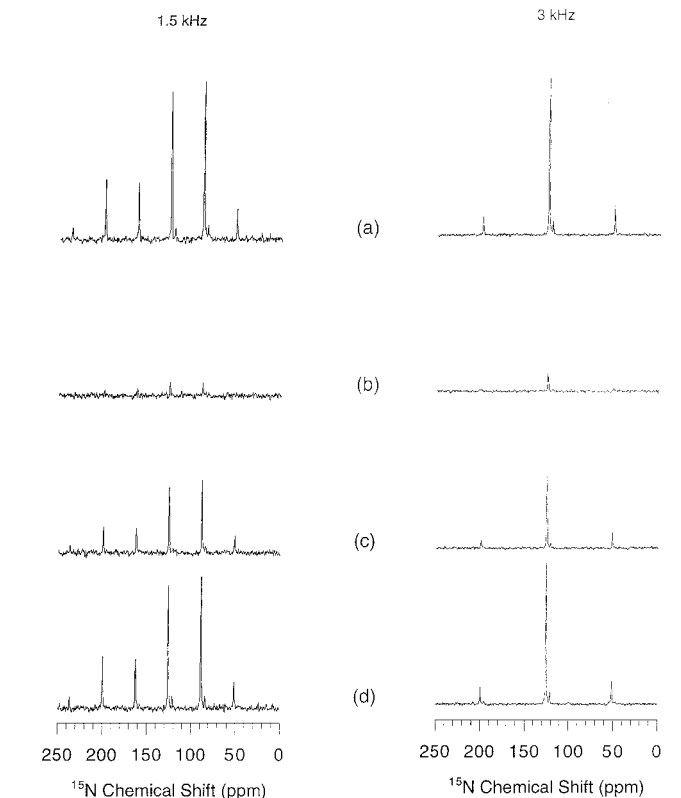
FIG. 11. Nitrogen-15 chemical shift spectra of a powder sample of N-acetyl-D,L-^{15}N-valine under MAS at a spinning speed of 1.5 kHz (left hand side) and 3.0 kHz (right hand side). The experimental conditions were the same as given in the caption of Fig. 10. (a) HH-match, (b) ^{15}N rf irradiation strength $b = 20.8$ kHz (with a 20.87-kHz mismatch), (c) ^{15}N irradiation during CP offset by 36.1 kHz, $b = 20.8$ kHz, with an effective field satisfying $a = \sqrt{b^2 + \Delta^2} = 41.67$ kHz, and (d) same as (c), but with a 60° post-CP pulse on ^{15}N spins in order to compensate the tilted effective field.
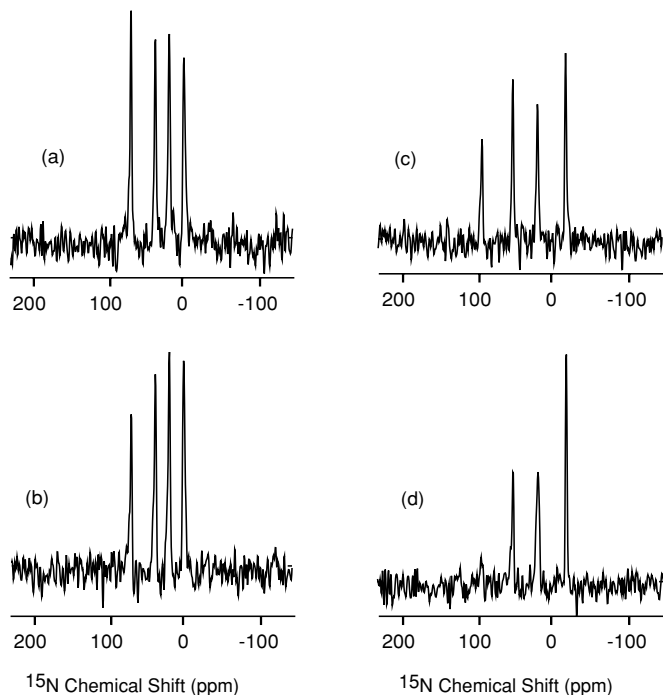
FIG. 12. Nitrogen-15 chemical shift spectra of a single crystal sample of N-acetyl-^{15}N-L-valyl-^{15}N-L-leucine. Spectra (a) and (b) were for the same unknown orientation (orientation A) of the crystal in the magnet. Spectra (c) and (d) were obtained from a different unknown orientation (orientation B). Experimental conditions used to obtain spectra (a) and (c) were same as in Fig. 11a, and spectra (b) and (d) were the same as in Fig. 11d.

5. CONCLUSIONS

The effect of CSA and rf offset on one of the spins in a system of dipolar coupled heteronuclear spin-$\frac{1}{2}$ pairs on the CP dynamics is investigated in an integrated fashion. Simulations aided by the analytical solutions are presented tracking the evolution of all possible coherence modes under various CP conditions together with plots of maximum possible CP as a function of the rf offset for oriented systems and powders. We discussed the effect of the relative orientation of the CSA and dipolar coupling tensors and the influence of powder averaging on CP dynamics. We identify an important feature of an offset is to in general slow down the rates of exchange amongst coherences belonging to the two spins. In addition we outline in detail how a double compensation procedure (rf offset and HH-mismatch on S-spin channel fulfilling the condition $a = \sqrt{b^2 + \Delta^2}$ during CP and a post-CP pulse compensating for the tilt of the resulting effective field) can be used to generate a CP signal akin to standard CP, albeit with reduced rf power during the CP period. Many of these aspects concerning the rich CP dynamics in the presence of offset and/or HH-mismatch were illustrated by static and MAS experiments on powder samples and static experiments on a single crystal. The slowdown of CP dynamics, hinted at by the experiments on the NAV powder sample, was confirmed with experiments on the single crystal of NAVL while the oscillatory nature of the underlying dynamics was uncovered as well.

REFERENCES

1. S. R. Hartmann and E. L. Hahn, *Phys. Rev.* **128,** 2042–2053 (1961).

2. A. Pines, M. G. Gibby, and J. S. Waugh, *J. Chem. Phys.* **59,** 569–590 (1973).

3. L. Muller, A. Kumar, T. Baumann, and R. R. Ernst, *Phys. Rev. Lett.* **32,** 1402–1406 (1974).

4. L. Muller and R. R. Ernst, *Mol. Phys.* **38,** 963–992 (1979).

5. M. H. Levitt, D. Suter, and R. R. Ernst, *J. Chem. Phys.* **84,** 4243–4255 (1986).

6. Elbayed and D. Canet, *Mol. Phys.* **71,** 979 (1990).

7. M. Ernst, B. H. Meier, M.Tomaselli, and A. Pines, *J. Chem. Phys.* **108,** 9611–9613 (1998).

8. X. Wu and K. W. Zilm, *J. Magn. Reson. A* **104,** 154–165 (1993).

9. M. Baldus, A. T. Petkova, J. Herzfeld, and R. G. Griffin, *Mol. Phys.* **95,** 1197–1207 (1998).

10. M. H. Levitt, *J. Chem. Phys.* **94,** 30–38 (1991).

11. B. H. Meier, *Chem. Phys. Lett.* **188,** 201–207 (1992).

12. S. Hediger, B. H. Meier, and R. R. Ernst, *Chem. Phys. Lett.* **213,** 627–635 (1993).

13. S. Zhang, B. H. Meier, S. Appelt, M. Mehring, and R. R. Ernst, *J. Magn. Reson. A* **101,** 60–66 (1993).

14. S. Hediger, B. H. Meier, N. D. Kurur, G. Bodenhausen, and R. R. Ernst, *Chem. Phys. Lett.* **223,** 283–288 (1994).

15. S. Hediger, B. H. Meier, and R. R. Ernst, *J. Chem. Phys.* **102,** 4000–4011 (1995).

16. M. Baldus, D. G. Geurts, S. Hediger, and B. H. Meier, *J. Magn. Reson. A* **118,** 140–144 (1996).

17. S. Hediger, P. Signer, M. Tomaselli, R. R. Ernst, and B. H. Meier, *J. Magn. Reson.* **125,** 291–301 (1997).

18. M. Baldus and B. H. Meier, *J. Magn. Reson.* **128,** 172–193 (1997).

19. R. Verel, M. Baldus, M. Ernst, and B. H. Meier, *Chem. Phys. Lett.* **287,** 421–428 (1998).

20. J. S. Waugh, *J. Magn. Reson.* **68,** 189–192 (1986).

21. K. Schmidt-Rohr and H. W. Spiess, "Multidimensional Solid-State NMR and Polymers," Academic Press, New York (1994).

22. T. Carlomagno, B. Luy, and S. J. Glaser, *J. Magn. Reson.* **126,** 110–119 (1997).

23. R. Fu, P. Pelupessy, and G. Bodenhausen, *Chem. Phys. Lett.* **264,** 63–69 (1997).

24. M. Mehring, "High-Resolution NMR of Solids," Springer-Verlag, Berlin (1983).

25. R. R. Ernst, G. Bodenhausen, and A. Wokaun, "Principles of Nuclear Magnetic Resonance in One and Two Dimensions," Clarendon, Oxford (1987).

26. S. C. Shekar and A. Ramamoorthy, *Chem. Phys. Lett.* **342,** 127–134 (2001).

27. A. Ramamoorthy and P. T. Narasimhan, *Mol. Phys.* **73,** 207–219 (1991).

28. D. K. Lee, Y. Wei, and A. Ramamoorthy, *J. Phys. Chem. B* **105,** 4752–4762 (2001).

29. D. K. Lee, J. S. Santos, and A. Ramamoorthy, *J. Phys. Chem. B* **103,** 8383–8390 (1999).

30. A. Ramamoorthy, C. H. Wu, and S. J. Opella, *J. Magn. Reson.* **140,** 131–140 (1999).

31. D. M. Taylor and A. Ramamoorthy, *J. Mol. Struct.* **602–603,** 115–124 (2002).

32. D. M. Taylor, "Nuclear Magnetic Resonance Coherence Transfer in a Homonuclear Two Spin-1/2 Solid-State System," Ph.D. Thesis, University of Michigan, Ann Arbor, MI (2001).

33. D. K. Lee, R. J. Wittebort, and A. Ramamoorthy, *J. Am. Chem. Soc.* **120,** 8868–8874 (1998).

34. Y. Wei, D. K. Lee, and A. Ramamoorthy, *J. Am. Chem. Soc.* **123,** 6118–6126 (2001).

35. J. R. Brender, D. M. Taylor, and A. Ramamoorthy, *J. Am. Chem. Soc.* **123,** 914–922 (2001).

36. A. Ramamoorthy, F. Marassi, and S. J. Opella, *J. Biomol. NMR*, **6,** 329 (1995); F. M. Marassi, A. Ramamoorthy, and S. J. Opella, *Proc. Natl. Acad. Sci. U. S. A.* **94,** 8551 (1997); A. Bax, B. L. Hawkins, and G. E. Maciel, *J. Magn. Reson.* **59,** 530–535 (1984).

37. S. C. Shekar, D. K. Lee, and A. Ramamoorthy, *J. Am. Chem. Soc.* **123,** 7467–7468 (2001).

38. M. Ravikumar and A. Ramamoorthy, *Chem. Phys. Lett.* **286,** 199–204 (1998).

39. O. B. Peersen, X. Wu, I. Kustanovich, and S. O. Smith, *J. Magn. Reson. A* **104,** 334–339 (1993).

40. Y. Ishii, J. Ashida, and T. Terao, *Chem. Phys. Lett.* **246,** 439–445 (1995).

41. I. Schnell, B. Langer, H. M. Sontjens, M. H. P. van Genderen, R. P. Sijbesma, and H. W. Spiess, *J. Magn. Reson.* **150,** 57–70 (2001).

42. K. Schmidt-Rohr, K. Saalwachter, S. F. Liu, and M. Hong, *J. Am. Chem. Soc.* **123,** 7168–7169 (2001).

43. Y. Ishii and R. Tycko, *J. Magn. Reson.* **142,** 199–204 (2000).

44. M. Hong and S. Yamaguchi, *J. Magn. Reson.* **150,** 43–48 (2001).

45. Y. Wei, K. J. Hallock, D. K. Lee, and A. Ramamoorthy, *Chem. Phys. Lett.* **351,** 42–46 (2002).